



# Sensing profiles of the volume scattering function at 180° using a single-photon oceanic fluorescence lidar

MINGJIA SHANGGUAN,\* YIRUI GUO, ZHUOYANG LIAO, AND ZHONGPING LEE

State Key Laboratory of Marine Environmental Science, College of Ocean and Earth Sciences, Xiamen University, Xiamen 361102, China

\*mingjia@xmu.edu.cn

**Abstract:** A novel oceanic fluorescence lidar technique has been proposed and demonstrated for remotely sensing the volume scattering function at 180° ( $\beta_f$ ), which can be used to further retrieve the profiles of the absorption coefficient of phytoplankton ( $a_{ph}$ ) at 532 nm and chlorophyll concentration (Chl). This scheme has these features. 1) The single-photon detection technology is employed to enhance the detection sensitivity to the single-photon level, enabling the oceanic lidar to obtain fluorescence backscatter profiles. 2) In terms of algorithms, the Raman backscattered signals of the water are utilized to normalize the backscattered signals of chlorophyll fluorescence, effectively minimizing the depth-dependent variation of the differential lidar attenuation coefficient ( $\Delta K_{lidar}^{fr}$ ). To reduce the contamination of fluorescence signals in the Raman backscatter signals, a Raman filter with a bandwidth of 6 nm was chosen. Subsequently, a perturbation method is utilized to invert the  $\beta_f$  of the fluorescence lidar. Finally,  $a_{ph}$  and Chl profiles can be inverted based on empirical models. 3) The value of  $\Delta K_{lidar}^{fr}$  used in inversion is obtained through a semi-analytic Monte Carlo simulation. According to theoretical analysis, the maximum relative error of  $\beta_f$  for Chl ranging from 0.01 mg/m<sup>3</sup> to 10 mg/m<sup>3</sup> is less than 13 %. To validate this approach, a field experiment was conducted aboard the R/V Tan Kah Kee in the South China Sea from September 4th to September 5th, 2022, resulting in continuous subsurface profiles of  $\beta_f$ ,  $a_{ph}$ , and Chl. These measurements confirm the robustness and reliability of the oceanic single-photon fluorescence lidar system and the inversion algorithm.

© 2023 Optica Publishing Group under the terms of the [Optica Open Access Publishing Agreement](#)

## 1. Introduction

Monitoring phytoplankton is vital for understanding their role in marine ecosystems, including their contribution to primary production, nutrient cycling, and the response to environmental changes. To monitor phytoplankton, various approaches have been developed, including laboratory measurements, in-situ monitoring, and remote sensing techniques. While laboratory measurements and in-situ monitoring can provide accurate results, they require significant human labor and are constrained by limited sampling points and frequencies. In contrast, remote sensing technology offers advantages in terms of spatial coverage and temporal resolution [1].

In the past few decades, the development of ocean color remote sensing technology has greatly expanded our understanding of marine phytoplankton, encompassing global-scale spatiotemporal characteristics, biomass, taxonomic composition, and productivity [2,3]. However, these measurements are limited to clear sky, day-light, high sun elevation angles, and are exponentially weighted toward the ocean surface [4]. The characteristics of lidar, including its three times greater penetration depth compared to ocean color, continuous day and night observation capability, high accuracy, and superior spatial and temporal resolution, make it a vital complement to passive remote sensing technologies [5].

Among them, laser-induced fluorescence lidar systems have been developed for oceanographic research and monitoring, including the detection of oil spills and other pollutants [6,7], quantification and characterization of phytoplankton and colored dissolved organic matter (CDOM) [8,9], as well as the estimation of total suspended matter (TSM) concentrations in the sea surface layer [9]. Furthermore, fluorescence lidar has been extensively tested in various environments, including the open ocean, coastal zones, estuaries, and lagoons, using different platforms like airborne, ship-mounted, and stationary systems [10]. However, it still has certain limitations. Due to the significantly weaker intensity of fluorescence signals compared to elastic scattering signals, existing oceanic lidar systems, despite using high-power lasers, can only obtain information from the surface layer of the water [8,11–14].

Fortunately, the single-photon detection technology provides the possibility of acquiring profiles of weak fluorescence backscattered signals, and it has already been applied in the fields of atmospheric and oceanic lidar [15–20]. The high sensitivity of single-photon detection technology enables long-range detection capabilities even with a low pulse energy laser and a small-aperture telescope. This advantage facilitates the miniaturization and high integration of lidar systems [18–20]. In this work, the single-photon detection technology is utilized to acquire fluorescence profiling data from a fluorescence lidar. Although photon-counting technology has been utilized for measuring fluorescence backscattered signals in water, this study employs a fiber-coupled optical receiver instead of spatially coupled one [21]. The utilization of a fiber-coupled configuration not only enhances system stability but also compresses the field of view (FOV) of the receiver, thereby suppressing multiple scattering components within the fluorescence backscattered signal, and ultimately benefiting the inversion process.

However, after obtaining the profiling data, it remains a challenge to retrieve the volume scattering function at  $180^\circ$  ( $\beta_f$ ) of the fluorescence lidar. This challenge arises from the fact that it faces an ill-posed mathematical problem, as it needs to infer two unknowns, namely, the lidar attenuation coefficient ( $K_{lidar}$ ) and  $\beta_f$ , from a single measurement. Numerous attempts have been made to resolve this inherent ill-posed problem in the lidar equation. Initially, various algorithms have been proposed without changing the mechanism of elastic backscatter lidar, including the slope method [22], Klett method [23], Fernald method [24] and perturbation method [25], among others. However, each method is based on a set of assumptions that may not be perfect, leading to certain levels of inverse error. Furthermore, the approach of incorporating a molecular channel or a Raman channel from water into the lidar system has been proposed, making the equation solvable [20,26].

In this work, considering the relative ease of implementation and maintenance compared to adding a molecular channel, it is decided to integrate a Raman channel alongside the fluorescence channel. Subsequently, due to the significantly reduced variation of the differential lidar attenuation coefficient ( $\Delta K_{lidar}^{fr}$ ) with depth, the perturbation method can be used to invert  $\beta_f$  [25]. Ultimately, the absorption coefficient of phytoplankton ( $a_{ph}$ ) at 532 nm and the concentration of chlorophyll (Chl) profiles can be inverted based on empirical models.

The article is organized as follows. Firstly, the methodology is introduced, which includes the derivation of formulas and the selection of Raman filter bandwidth. Next, an analysis is conducted on the range and selection of the  $\Delta K_{lidar}^{fr}$ , where the range is determined through a Monte Carlo (MC) method, and the errors resulting from the selection of  $\Delta K_{lidar}^{fr}$  in the inversion process are analyzed. Subsequently, an error analysis of the proposed algorithm is conducted using four different Chl vertical distributions. Finally, a field experiment is presented to validate the robustness and feasibility of both the algorithm and the lidar system.

## 2. Methodology

### 2.1. Derivation of formulas

The backscatter profile of the fluorescence lidar can be expressed as follows [27]:

$$P_f(\lambda_f, \sigma_f, z) = \frac{B_f \cdot Q_f(z)}{(n \cdot H + z)^2} \cdot \beta_f(\lambda_f, z) \otimes g(\lambda_f, \sigma_f) \cdot \exp \left\{ - \int_0^z [K_{lidar}^m(y) + K_{lidar}^f(y)] dy \right\}, \quad (1)$$

where  $P_f$  represents the water fluorescence backscattered signal at a depth of  $z$ , given an emitted laser wavelength ( $\lambda_L$ ) of 532 nm and a fluorescence wavelength ( $\lambda_f$ ) of 685 nm;  $H$  represents the height at which the lidar is positioned above the water surface, which, in this case, is 15 m;  $n$  represents the refractive index indicator of the water;  $B_f$  is a constant that includes lidar parameters independent of depth, such as the output laser power, quantum efficiency of the detector, and transmittance of the optical transceiver system;  $Q_f(z)$  represents geometric overlap factor;  $\beta_f$  represents the volume scattering function at 180° for chlorophyll fluorescence at a wavelength of 685 nm;  $g(\lambda_f, \sigma_f)$  represents the transmittance function of a fluorescence filter, which can be approximated as a Gaussian function with a center wavelength of  $\lambda_f$  and a bandwidth of  $\sigma_f$ ;  $K_{lidar}^m$  represents the lidar attenuation coefficient at 532 nm;  $K_{lidar}^f$  represents the lidar attenuation coefficient at 685 nm.

Furthermore, the backscatter profile of the Raman channel from water can be expressed as follows:

$$P_r(\lambda_r, \sigma_r, z) = \frac{B_r \cdot Q_r(z)}{(n \cdot H + z)^2} \cdot \beta_r(\lambda_r, z) \otimes g(\lambda_r, \sigma_r) \cdot \exp \left\{ - \int_0^z [K_{lidar}^m(y) + K_{lidar}^r(y)] dy \right\}, \quad (2)$$

where  $P_r$  represents the backscattered water Raman signal at a depth of  $z$  when the emitted laser wavelength ( $\lambda_L$ ) is 532 nm and the Raman wavelength ( $\lambda_r$ ) is 650 nm;  $B_r$  is a constant that includes lidar parameters independent of depth, such as the output laser power, quantum efficiency of the detector, and transmittance of the optical transceiver system;  $Q_r(z)$  represents geometric overlap factor of the Raman channel. Since the Raman channel and the fluorescence channel share the same set of transceiver optical systems,  $Q_r(z) = Q_f(z)$ ;  $\beta_r$  represents the volume scattering function at 180° for a wavelength of 650 nm, encompassing the volume scattering function at 180° of water Raman at 650 nm ( $\beta_r$ ), as well as the contribution of chlorophyll fluorescence to the volume scattering function at 180° at that wavelength ( $\beta_f$ ), i.e.,  $\beta_r = \beta_r + \beta_f$ ;  $g(\lambda_r, \sigma_r)$  represents the transmittance function of the Raman filter, which can be approximated as a Gaussian function with a center wavelength of  $\lambda_r$  and a bandwidth of  $\sigma_r$ ;  $K_{lidar}^r$  represents the lidar attenuation coefficient at 650 nm.

According to an empirical model [28], the  $\beta_r$  can be expressed as follows:

$$\beta_r(\lambda_r) = b_R(\lambda_L, \lambda_r) \cdot f_R(\lambda_L, \lambda_r) \cdot \tilde{\beta}_R(\pi), \quad (3)$$

where  $b_R$  represents the Raman scattering coefficient of water molecules when the emitted laser wavelength ( $\lambda_L$ ) is 532 nm and the received Raman wavelength ( $\lambda_r$ ) is 650 nm;  $f_R$  represents the Raman wavelength distribution function;  $\tilde{\beta}_R(\pi)$  represents the Raman scattering phase function.

Firstly, by normalizing the fluorescence backscattered signal with the Raman backscattered signal, the resulting  $S_{fr}$  can be expressed as follows:

$$\begin{aligned} S_{fr}(\lambda_f, \lambda_r, z) &= \frac{B_f \cdot Q_f}{B_r \cdot Q_r} \cdot \frac{\beta_f(\lambda_f, z) \otimes g(\lambda_f, \sigma_f)}{\beta_r(\lambda_r, z) \otimes g(\lambda_r, \sigma_r)} \cdot \exp \left\{ - \int_0^z [K_{lidar}^f(y) - K_{lidar}^r(y)] dy \right\} \\ &= \frac{B_f}{B_r} \cdot \frac{\beta_f(\lambda_f, z) \otimes g(\lambda_f, \sigma_f)}{\beta_r(\lambda_r, z) \otimes g(\lambda_r, \sigma_r)} \cdot \exp \left[ - \int_0^z \Delta K_{lidar}^{fr}(y) dy \right] \end{aligned}, \quad (4)$$

where  $\Delta K_{lidar}^{fr} = K_{lidar}^f - K_{lidar}^r$ .

By normalizing, the variation of  $\Delta K_{lidar}^{fr}$  with depth is significantly reduced, enabling the utilization of a perturbation method for measuring the  $\beta_f$  [25]. As a result,  $S_{fr}$  can be decomposed into two parts: the depth-dependent component and the depth-independent component:

$$S_{fr}(z) = \frac{B_f}{B_r} \cdot \frac{[\beta_f(\lambda_f, z_0) + \beta'_f(\lambda_f, z)] \otimes g(\lambda_f, \sigma_f)}{[\beta_t(\lambda_r, z_0) + \beta'_t(\lambda_r, z)] \otimes g(\lambda_r, \sigma_r)} \cdot \exp \left[ -\Delta K_{lidar}^{fr0} \cdot z - \int_0^z \Delta K_{lidar}^{fr'}(y) dy \right], \quad (5)$$

where  $\beta_f(\lambda_f, z_0)$ ,  $\beta_t(\lambda_r, z_0)$ , and  $\Delta K_{lidar}^{fr0}$  respectively represent the components of  $\beta_f$ ,  $\beta_t$  and  $\Delta K_{lidar}^{fr}$  that do not vary with depth;  $\beta'_f(\lambda_f, z)$ ,  $\beta'_t(\lambda_r, z)$  and  $\Delta K_{lidar}^{fr'}(z)$  represent the components of  $\beta_f$ ,  $\beta_t$ , and  $\Delta K_{lidar}^{fr}$  that do vary with depth;  $z_0$  is the depth of the first point of the measured water signal.

When the depth-dependent term is ignored, the normalized signal  $S_{fr0}$  can be expressed as follows:

$$\begin{aligned} S_{fr0}(\lambda_f, \lambda_r, z) &= \frac{B_f}{B_r} \cdot \frac{\beta_f(\lambda_f, z_0) \otimes g(\lambda_f, \sigma_f)}{\beta_t(\lambda_r, z_0) \otimes g(\lambda_r, \sigma_r)} \exp(-\Delta K_{lidar}^{fr0} z) \\ &= \frac{S_{fr}(\lambda_f, \lambda_r, z_0)}{\exp[-\Delta K_{lidar}^{fr0} \cdot z_0]} \cdot \exp(-\Delta K_{lidar}^{fr0} z). \end{aligned} \quad (6)$$

It is worth noting that after determining the ratio  $B_f/B_r$  through experimental calibration, the value of  $\beta_f(\lambda_f, z_0) \otimes g(\lambda_f, \sigma_f) / \beta_t(\lambda_r, z_0) \otimes g(\lambda_r, \sigma_r)$  can be expressed as follows:

$$\frac{\beta_f(\lambda_f, z_0) \otimes g(\lambda_f, \sigma_f)}{\beta_t(\lambda_r, z_0) \otimes g(\lambda_r, \sigma_r)} = \frac{S_{fr}(\lambda_f, \lambda_r, z_0)}{\exp[-\Delta K_{lidar}^{fr0} \cdot z_0]} \cdot \frac{B_r}{B_f}. \quad (7)$$

According to the perturbation method [25], assuming  $\Delta K_{lidar}^{fr'} = 0$ ,  $\beta_f$  can be expressed as follows, based on Eq. (5) and Eq. (6):

$$\begin{aligned} \beta_f(\lambda_f, z) \otimes g(\lambda_f, \sigma_f) &= \frac{\beta_t(\lambda_r, z) \otimes g(\lambda_r, \sigma_r)}{\beta_t(\lambda_r, z_0) \otimes g(\lambda_r, \sigma_r)} \cdot \beta_f(\lambda_f, z_0) \otimes g(\lambda_f, \sigma_f) \cdot \frac{S_{fr}(\lambda_f, \lambda_r, z)}{S_{fr0}(\lambda_f, \lambda_r, z)} \\ &= \beta_t(\lambda_r, z) \otimes g(\lambda_r, \sigma_r) \cdot \frac{S_{fr}(\lambda_f, \lambda_r, z_0)}{\exp[-\Delta K_{lidar}^{fr0} \cdot z_0]} \cdot \frac{B_r}{B_f} \cdot \frac{S_{fr}(\lambda_f, \lambda_r, z)}{S_{fr0}(\lambda_f, \lambda_r, z)}. \end{aligned} \quad (8)$$

Finally, by deconvolving  $g(\lambda_f, \sigma_f)$  from Eq. (8), the expression for  $\beta_f$  can be obtained as follows:

$$\beta_f(\lambda_f, z) = \mathcal{F}^{-1} \left\{ \mathcal{F} \left[ \beta_t(\lambda_r, z) \otimes g(\lambda_r, \sigma_r) \cdot \frac{S_{fr}(\lambda_f, \lambda_r, z_0)}{\exp[-\Delta K_{lidar}^{fr0} \cdot z_0]} \cdot \frac{B_r}{B_f} \right] / \mathcal{F}[g(\lambda_f, \sigma_f)] \right\} \cdot \frac{S_{fr}(\lambda_f, \lambda_r, z)}{S_{fr0}(\lambda_f, \lambda_r, z)} \quad (9)$$

where  $\mathcal{F}$  and  $\mathcal{F}^{-1}$  respectively represent the Fourier transform and the inverse Fourier transform.

Define the coefficient  $\beta_{f0}^*(\sigma_r, \sigma_f, z)$  as

$$\beta_{f0}^*(\sigma_r, \sigma_f, z) = \mathcal{F}^{-1} \left\{ \mathcal{F} \left[ \beta_t(\lambda_r, z) \otimes g(\lambda_r, \sigma_r) \cdot \frac{S_{fr}(\lambda_f, \lambda_r, z_0)}{\exp[-\Delta K_{lidar}^{fr0} \cdot z_0]} \cdot \frac{B_r}{B_f} \right] / \mathcal{F}[g(\lambda_f, \sigma_f)] \right\}. \quad (10)$$

Then, the inversion result can be expressed as follows:

$$\beta_f(\lambda_f, z) = \beta_{f0}^*(\sigma_r, \sigma_f, z) \cdot \frac{S_{fr}(\lambda_f, \lambda_r, z)}{S_{fr0}(\lambda_f, \lambda_r, z)} \quad (11)$$

Ignoring fluorescence caused by substances other than chlorophyll in water, the inversion of  $a_{ph}$  and Chl can be further carried out using  $\beta_f$ . Firstly,  $\beta_f$  can be expressed as follows [29]:

$$\beta_f(\lambda_f, z) = a_{ph}[\lambda_L, z] \Phi_c \frac{\lambda_L}{\lambda_f} h_c(\lambda_f) \frac{1}{4\pi}, \quad (12)$$

where  $a_{ph}$  is the chlorophyll fluorescence absorption coefficient at an excitation wavelength of 532 nm;  $\Phi_c$  is the quantum yield of chlorophyll fluorescence, which is affected by factors such as

light, nutrients and temperature;  $h_c$  is the normalized emission wavelength function of chlorophyll fluorescence, which can be expressed using a model [30]. By utilizing Eq. (12) and substituting empirical values for  $\Phi_c$  and the model for  $h_c$ , the expression for  $a_{ph}$  can be obtained as follows:

$$a_{ph}(\lambda_L, z) = \beta_f(\lambda_f, z) / \left[ \Phi_c \frac{\lambda_L}{\lambda_f} h_c(\lambda_f) \frac{1}{4\pi} \right]. \quad (13)$$

Once  $a_{ph}$  is obtained, the Chl profile can be obtained by utilizing an empirical model for Chl [31]. Finally, the distribution of Chl can be obtained as follows:

$$\text{Chl}(z) = \exp \left\{ \frac{\ln[a_{ph}(\lambda_L, z)] - \ln(0.0113)}{0.871} \right\}. \quad (14)$$

To provide a clearer representation of the inversion process, the flowchart is illustrated in Fig. 1.

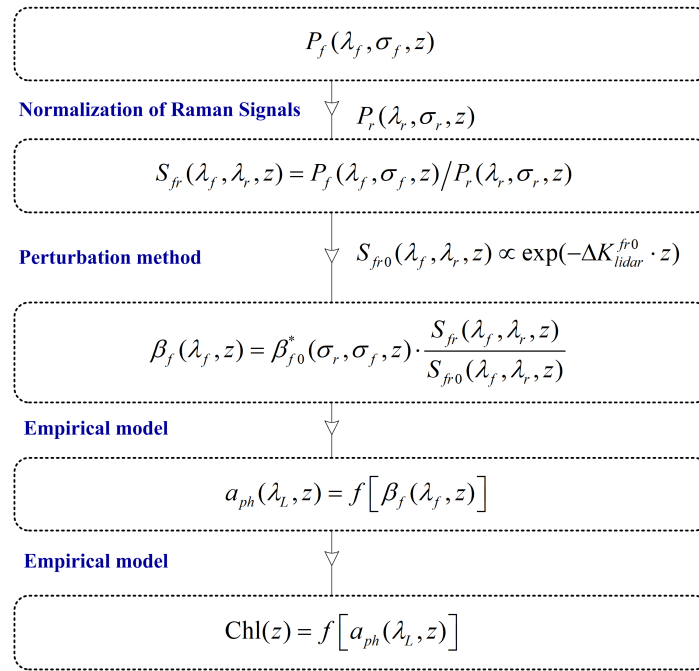


Fig. 1. Flowchart of the inversion process.

## 2.2. Selection the bandwidth of filters

From Eq. (11), it can be observed that in order to achieve accurate inversion of  $\beta_f$ , it is desirable to minimize the variation of  $\beta_{f0}^*$  with depth. Firstly, according to Eq. (10), the bandwidth of the fluorescence filter does not directly impact the value of  $\beta_{f0}^*$ . However, a larger bandwidth allows for a stronger reception of fluorescent backscattered signals and results in a higher signal-to-noise ratio (SNR) for detection. Therefore, employing a fluorescence filter with a larger bandwidth is desirable. However, due to the utilization of highly sensitive single-photon detectors and the presence of background noise interference, such as signal lights on the research vessel and moonlight, the wider the bandwidth, the stronger the background noise. A wider bandwidth can

also lead to interference from fluorescence signals induced by other substances, such as oil [32]. Therefore, a 10 nm bandwidth was selected in this study. When the background noise on the platform is low and the fluorescence signals caused by other substances can be ignored, a larger bandwidth for the fluorescence filter can be considered.

Furthermore, Eq. (10) indicates that  $\beta_{f_0}^*$  is influenced by the bandwidth of the Raman filter. Similar to the selection of the bandwidth for the fluorescence filter, a wider bandwidth for the Raman filter leads to a stronger Raman signal and a higher SNR, which is advantageous for detection. As shown in Fig. 2(a), a larger bandwidth results in a larger  $\beta_{ig}$  (where  $\beta_{ig} = \beta_t(\lambda_r, z) \otimes g(\lambda_r, \sigma_r)$ ) and a stronger return signal. Specifically, increasing the bandwidth from 6 nm to 10 nm leads to a  $\sim 1.5$ -fold enhancement in the signal strength.

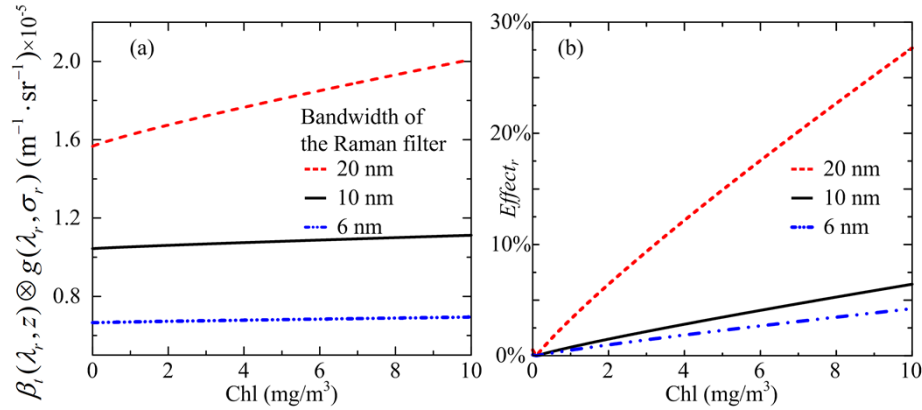


**Fig. 2.** (a) The variation of  $\beta_t(\lambda_r, z) \otimes g(\lambda_r, \sigma_r)$  with depth when the range of Chl from  $0.01 \text{ mg/m}^3$  to  $10 \text{ mg/m}^3$ , (b) The variation of  $Effect_r$  with depth when the reference value is  $\beta_t(\lambda_r, z_0) \otimes g(\lambda_r, \sigma_r)$ .

However, a wider bandwidth increases the sensitivity of the Raman signal to changes in Chl, resulting in the variation of  $\beta_{ig}$  in Eq. (10) with Chl. As illustrated in Fig. 2(a), it can be observed that a narrower bandwidth of the Raman filter leads to less variation in  $\beta_{ig}$  with Chl, which is particularly crucial for detecting chlorophyll-stratified water.

To quantify the relative change in  $\beta_{ig}$  caused by the variation in Chl,  $Effect_r$  is defined as follows

$$Effect_r = \left| \frac{\beta_t(\lambda_r, z) \otimes g(\lambda_r, \sigma_r) - \beta_t(\lambda_r, z_0) \otimes g(\lambda_r, \sigma_r)}{\beta_t(\lambda_r, z_0) \otimes g(\lambda_r, \sigma_r)} \right| \times 100 \%. \quad (15)$$

As shown in Fig. 2(b), when the Raman bandwidth is selected to be 6 nm, the range of  $Effect_r$  is changes by only 4.3% when the Chl changes from  $0.01 \text{ mg/m}^3$  to  $10 \text{ mg/m}^3$ . To strike a balance with the aforementioned tradeoff, a bandwidth of 6 nm is selected for the Raman filter.

Due to the minimal variation in  $\beta_{ig}$  with Chl, it is possible to assume that  $\beta_{ig}$  is approximately equal to  $\beta_r(\lambda_r) \otimes g(\lambda_r, \sigma_r)$ . Therefore, Eq. (10) can be rewritten as follows:

$$\beta_{f_0}^*(\sigma_r, \sigma_f) = \mathcal{F}^{-1} \left\{ \mathcal{F} \left[ \beta_r(\lambda_r) \otimes g(\lambda_r, \sigma_r) \cdot \frac{S_{fr}(\lambda_f, \lambda_r, z_0)}{\exp(-\Delta K_{lidar}^{fr0} \cdot z_0)} \cdot \frac{B_r}{B_f} \right] / \mathcal{F}[g(\lambda_f, \sigma_f)] \right\}. \quad (16)$$

### 3. Variation range and determination of $\Delta K_{lidar}^{fr0}$

#### 3.1. Variation range of $\Delta K_{lidar}^{fr0}$

From Eq. (6), the inversion of  $\beta_f$  requires prior knowledge of the  $\Delta K_{lidar}^{fr0}$  value. This value is influenced not only by the hardware parameters of the lidar system but also by the inherent optical

properties (IOPs) of the water, as well as the multiple scattering of laser light by particles in water. To determine the variation range of  $\Delta K_{lidar}^{lr0}$  value, this study utilizes a MC simulation, which is widely recognized as a crucial tool for simulating complex processes and has been extensively employed in simulating the backscattered signal of oceanic lidars [33]. In this study, a brief introduction to MC-based simulation of backscattered signals in fluorescence lidar is provided without delving into specific details. For a more comprehensive understanding of the simulation process, it is recommended to refer to a recent article [27].

The MC is used to simulate the random trajectories of photon propagation in a medium. The step and direction of photon trajectories depend on the scattering and absorption properties of the medium. Meanwhile, the MC method treats the photon as a typical particle and ignores its wave properties. The propagation of laser in water is treated as the combination of many photon trajectories. Laser energy attenuation is determined by three factors, namely the absorption of the medium, the scattering probability, and the probability distribution of the steps. To enhance the utilization efficiency of individual photons, a semi-analytic MC model is applied [27]. This model allows for the calculation of the expected energy value and position recording of each photon within the FOV of the telescope. The hardware parameters of the lidar used in the simulation are based on the actual shipborne single-photon fluorescence lidar, as shown in Table 1. The bio-optical models used in the simulation are presented in Table 2.

**Table 1. Hardware parameters of the lidar system**

	Parameter	Value
Pulsed laser	Radius of laser beam	2 mm
	Laser divergence angle	0.5 mrad
Coupler	Diameter of telescope	22 mm
	FOV of the telescope	2.1 mrad
Scattering phase function	Petzold phase function [34]	
Other parameters	Number of photons	$10^8$
	Sampling interval	100 mm

**Table 2. The bio-optical models used in the MC simulation**

Empirical relationships	Applicable range of Chl	References
$\begin{cases} a_y(\lambda) = a_y(440) \exp[-0.014(\lambda - 440)] \\ a_y(440) = 0.2[a_w(440) + 0.06A(440) \cdot \text{Chl}^{0.65}] \end{cases}$	0.02-20 mg/m <sup>3</sup>	[35]
$b_w(\lambda) = 0.0046(450/\lambda)^{4.32}$	-	[36]
$b_R(\lambda) = 2.6 \times 10^{-4}(488/\lambda)^{5.5}$	-	[37]
$b_p(\lambda) = 0.3\text{Chl}^{0.62}(550/\lambda)$	0.03-30 mg/m <sup>3</sup>	[38]

The absorption and scattering coefficients are modeled as follows:

$$a(\lambda) = a_w(\lambda) + 0.06A(\lambda) \cdot \text{Chl}^{0.65} + a_y(\lambda), \quad (17)$$

$$b(\lambda) = b_w(\lambda) + b_p(\lambda), \quad (18)$$

where  $a_w$  is the absorption coefficient of pure seawater [38],  $A$  is the normalized spectral absorption values of phytoplankton pigments,  $a_y$  is the absorption coefficient of yellow substance,  $b_w$  is the scattering coefficient of pure water [36].

In the simulations, a widely used Petzold phase function was adopted [34]. With a sampling length of 20 m and a sampling interval of 0.1 m, a total of 200 sampling points can be obtained.

As shown in Fig. 3(a) and (c), the simulated fluorescence backscattering signal and the Raman backscattering signal decays exponentially. To mitigate the effects of multiple scattering in the lidar backscatter signal, a small-aperture telescope with a narrow FOV is used.

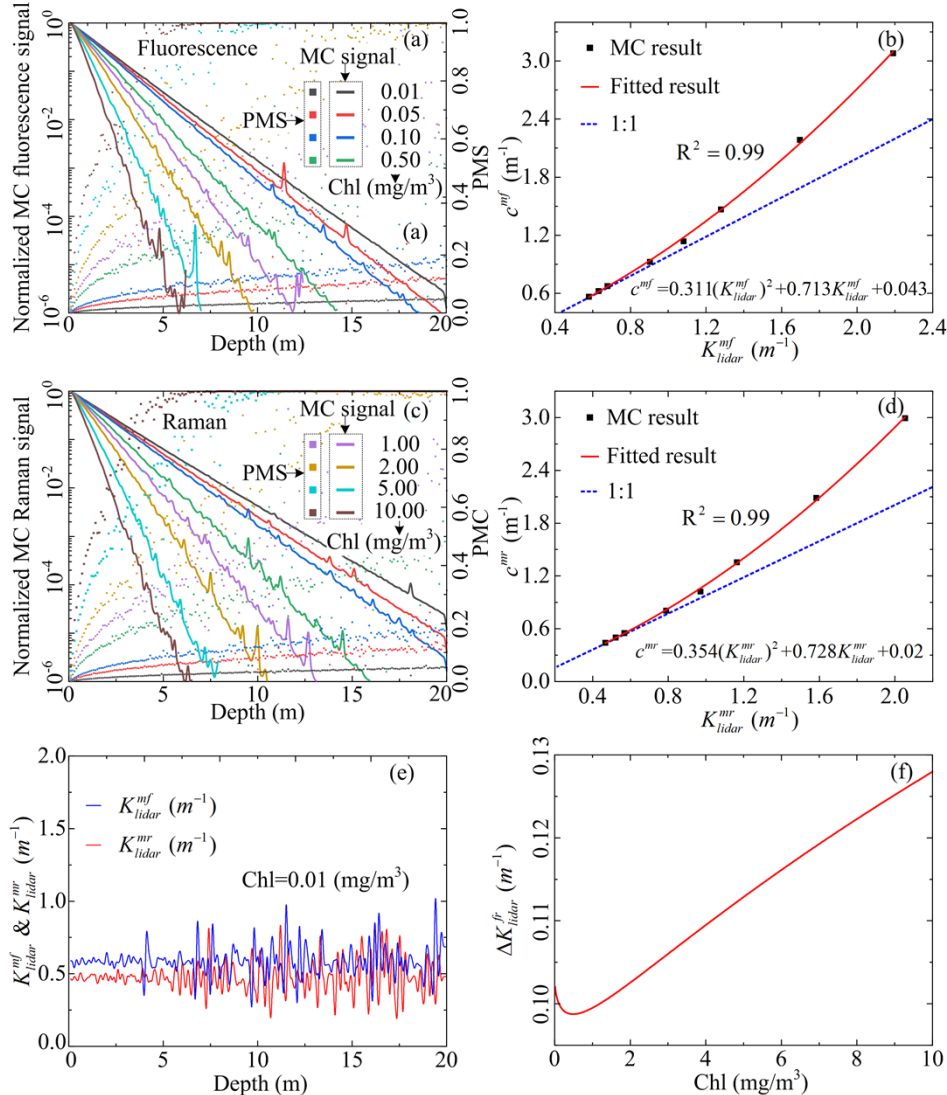


**Fig. 3.** (a) Simulate fluorescence backscattered signals (lines) and the percentage of multiple scattering (PMS) in the signals (scatters) for Chl ranging from 0.01 to 10  $\text{mg}/\text{m}^3$  using the Petzold phase function. (b) Relationships between  $K_{lidar}^{mf}$  and  $c^{mf}$ , where scatter represents the results of MC simulations, and the solid line represents the fitted results. (c) and (d) same as (a) and (b), but for Raman backscattered signals. (e) Vertical profile of  $K_{lidar}^{mf}$  and  $K_{lidar}^{mr}$  when Chl is 0.01  $\text{mg}/\text{m}^3$ . (f) The values of  $\Delta K_{lidar}^{fr}$  for varying Chl ranging from 0.01 to 10  $\text{mg}/\text{m}^3$ .

As shown in Fig. 3(a) and Fig. 3(c), when the Chl is low, the percentage of multiple scattering (PMS), which includes secondary scattering and higher-order scattering, is low. Consequently, the lidar signal is predominantly governed by single scattering. Taking the example of a Chl of

0.01 mg/m<sup>3</sup>, as shown in Fig. 3(e), the attenuation coefficient profile of the lidar exhibit relatively stable within a 20 m range, despite increased variability with increasing depth due to lower SNR. However, as the Chl increases, the PMS increases. Afterwards,  $K_{lidar}^{mf}$  and  $K_{lidar}^{mr}$  at different Chl is obtained by selecting the original signal with a PMS less than 100% and using the slope method [18]. The relationship between  $K_{lidar}^{mf}$  and  $c^{mf}$  for the Chl ranging from 0.01 to 10 mg/m<sup>3</sup> is shown in Fig. 3(b), and the relationship between  $K_{lidar}^{mr}$  and  $c^{mr}$  is shown in Fig. 3(d). Subsequently, the relationship between  $K_{lidar}^{mf}$  and  $c^{mf}$ , as well as  $K_{lidar}^{mr}$  and  $c^{mr}$ , for the fluorescence and Raman channels, respectively, is fitted using a second-order polynomial. The fitting results are shown in Fig. 3(b) and 3(d), with a high degree of correlation indicated by the R-Square ( $R^2$ ) value of 0.99 for both channels. The conclusion is consistent with the finding that  $K_{lidar}$  tends to closely align with the beam attenuation coefficient ( $c$ ) when the lidar backscattered signal is predominantly governed by quasi-single scattering, whereas  $K_{lidar}$  is given by the diffuse attenuation coefficient ( $K_d$ ) when the backscattered signal is primarily influenced by multi-scattering [30]. Ultimately, the difference between  $K_{lidar}^{mf}$  and  $K_{lidar}^{mr}$ , referred to as  $\Delta K_{lidar}^{fr}$ , is shown in Fig. 3(f) within the range of Chl from 0.01 to 10 mg/m<sup>3</sup>. From Fig. 3(f), it can be observed that the values of  $\Delta K_{lidar}^{fr}$  range between 0.10 and 0.13.

### 3.2. Determination of the value of $\Delta K_{lidar}^{fr0}$

From Eq. (6), it is evident that the deviation of  $\Delta K_{lidar}^{fr0}$  results in errors in the calculation of  $S_{fr0}$ . Therefore, the next step is to first evaluate the errors introduced by the deviation in  $\Delta K_{lidar}^{fr0}$ .

By defining  $\Delta K_{lidar}^{fr0}$  used in the inversion process as  $\Delta K_{lidar}^{fr0'}$ , the inverted values of  $S_{fr0}$  and  $\beta_f$  obtained based on this value can be expressed as  $S'_{fr0}$  and  $\beta'_f$ , respectively, as shown below:

$$S'_{fr0}(\lambda_f, \lambda_r, z) = \frac{\exp(-\Delta K_{lidar}^{fr0'} \cdot z)}{\exp[-\Delta K_{lidar}^{fr0} \cdot z_0]} \cdot S_{fr}(\lambda_f, \lambda_r, z_0), \quad (19)$$

$$\beta'_f(\lambda_f, z) = \frac{S_{fr}(\lambda_f, \lambda_r, z)}{S'_{fr0}(\lambda_f, \lambda_r, z)} \cdot \beta_{f0}^*(\sigma_r, \sigma_f). \quad (20)$$

The error introduced by the deviation in  $\Delta K_{lidar}^{fr0}$  is defined as  $Error_1$ , which can be expressed as follows:

$$Error_1 = \left| \frac{\beta'_f(\lambda_f, z) - \beta_f(\lambda_f, z)}{\beta_f(\lambda_f, z)} \right| \times 100\%. \quad (21)$$

From Eq. (19) to Eq. (20),  $Error_1$  can get can be further expressed as:

$$\begin{aligned} Error_1 &= \left| \frac{\beta_{f0}^*(\sigma_r, \sigma_f) \cdot \frac{S_{fr}(\lambda_f, \lambda_r, z)}{S'_{fr0}(\lambda_f, \lambda_r, z)} - \beta_{f0}^*(\sigma_r, \sigma_f) \cdot \frac{S_{fr}(\lambda_f, \lambda_r, z)}{S_{fr0}(\lambda_f, \lambda_r, z)}}{\beta_{f0}^*(\sigma_r, \sigma_f) \cdot \frac{S_{fr}(\lambda_f, \lambda_r, z)}{S_{fr0}(\lambda_f, \lambda_r, z)}} \right| \\ &= \left| \frac{S_{fr0}(\lambda_f, \lambda_r, z) - S'_{fr0}(\lambda_f, \lambda_r, z)}{S'_{fr0}(\lambda_f, \lambda_r, z)} \right| = \left| \frac{\exp(-\Delta K_{lidar}^{fr0} \cdot z) - \exp(-\Delta K_{lidar}^{fr0'} \cdot z)}{\exp(-\Delta K_{lidar}^{fr0'} \cdot z)} \right| \times 100\% \end{aligned} \quad (22)$$

As calculated in the previous section, when the Chl varies from 0.01 mg/m<sup>3</sup> to 10 mg/m<sup>3</sup>, the range of  $\Delta K_{lidar}^{fr}$  is from 0.1 to 0.13. Substituting this range of  $\Delta K_{lidar}^{fr}$  into Eq. (22),  $Error_1$  at different depths can be obtained, as shown in Fig. 4 (a) to (d), the results are provided for depths of 1 m, 5 m, 10 m, and 20 m, respectively. From these results, it can be observed that the  $Error_1$  increases with larger deviations of  $\Delta K_{lidar}^{fr}$  and deeper depths. However, within the detection range of the lidar system used in this study (up to a depth of 10 m), when is set to

$\Delta K_{lidar}^{fr0}$  0.11, the error remains within 15%. Therefore, in the subsequent inversion process, the value of  $\Delta K_{lidar}^{fr0}$  is set to 0.11.

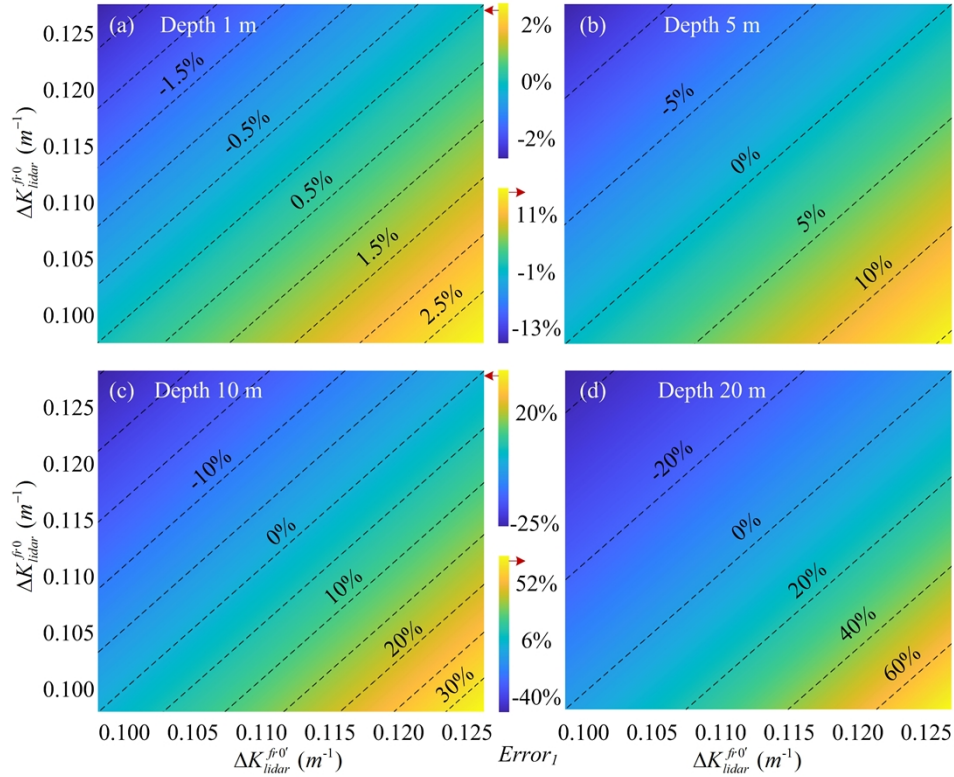


**Fig. 4.**  $Error_1$  distribution for deviation of  $\Delta K_{lidar}^{fr0}$  at depths of 1 m (a), 5 m (b), 10 m (c), and 20 m (d).

#### 4. Inversion error analysis

Next, the errors caused by the inversion algorithm will be systematically analyzed. It should be noted that this analysis exclusively focuses on the errors originating from the inversion algorithm, while excluding errors that arise from the SNR of the lidar backscatter signal. Four typical vertical distribution models of Chl will be used for analysis, representing open-ocean, mid-latitude case 1 water, lakes, and water surrounding Europe [39–42]. The vertical distribution characteristics of these four Chl profiles are presented in Table 3 and their respective vertical profile curves are shown in Fig. 5.

**Table 3. Vertical distribution model of Chl**

Vertical distribution model	References
$Chl(z) = -0.03z + 0.4$	[39]
$Chl(z) = 0.01z + 0.1$	[40]
$Chl(z) = 9.5 \exp \left[ \frac{-(z-2)^2}{2 \cdot (2/2.355)^2} \right] + 0.5$	[41]
$Chl(z) = 1.5 \exp \left[ \frac{-(z-3)^2}{2 \cdot (2/2.355)^2} \right] + 9.5 \exp \left[ \frac{-(z-6)^2}{2 \cdot (2/2.355)^2} \right] + 0.5$	[42]

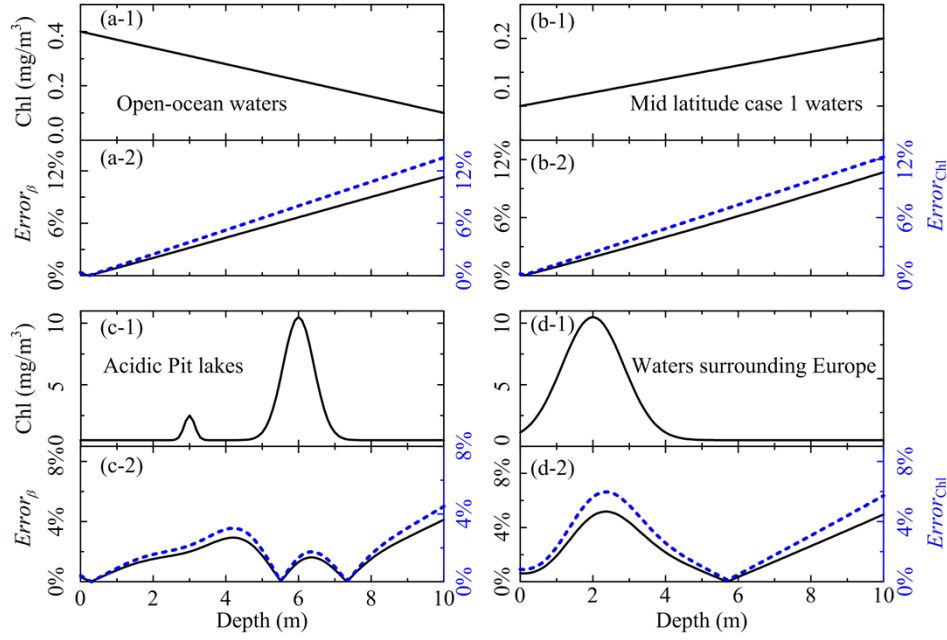


**Fig. 5.** Inversion errors under different vertical distributions of Chl. The sub-figures (a)-(d) show different Chl vertical distribution: (a) linearly decreasing [39], (b) linearly increasing [40], (c) bimodal with two Gaussian distribution [42], and (d) unimodal with a single Gaussian distribution [41]. Each sub-figure comprises two panels: the top panel displays the corresponding Chl vertical distribution, while the bottom panel shows the distribution of  $Error_{\beta}$  and  $Error_{Ch1}$ .

To calculate the errors, the lidar backscattered signal is constructed based on the vertical distribution of Chl. Firstly, based on the four vertical distribution models of Chl from Table 3, the beam attenuation coefficients  $c^m$  and  $c^f$  are calculated using the bio-optical model from Table 2, employing Eq. (17) and Eq. (18). Subsequently, the relationship between the combined attenuation coefficient  $c^{mf}$  ( $c^{mf} = c^m + c^f$ ) and the lidar attenuation coefficient  $K_{lidar}^{mf}$  is established using MC simulation, as described in Section 3.1, resulting in the vertical profile of  $K_{lidar}^{mf}$ . Furthermore,  $\beta_f$  is calculated using the vertical distribution of Chl and Eq. (12) with the values of  $\Phi_c$  of 0.06. Similarly, by applying the same methodology used to calculate  $K_{lidar}^{mf}$ , the vertical profile of  $K_{lidar}^{mr}$  can be obtained. The coefficient  $\beta_t$  of the Raman channel can be obtained by using Eq. (3) and Eq. (12). Given the reconstruction of  $K_{lidar}^{mf}$  and  $\beta_f$ , as well as the reconstruction of  $K_{lidar}^{mr}$  and  $\beta_t$ , along with the assumptions of  $B_f$  and  $B_r$ , and the knowledge of  $Q_f(z)$  and  $Q_r(z)$ ,  $P_f$  and  $P_r$  can be reconstructed using Eq. (1) and Eq. (2).

Subsequently, the inversion method detailed in Section 2 is employed to invert  $\beta_f$  and Chl, with the value of  $\Delta K_{lidar}^{fr0}$  set to 0.11. Finally, the respective deviations from the true values, denoted as  $Error_{\beta}$  (for  $\beta_f$ ) and  $Error_{Ch1}$  (for Chl), can be calculated using the following equations:

$$Error_{\beta} = \left| \frac{\beta_f(z) - \beta_f^{st}(z)}{\beta_f^{st}(z)} \right| \times 100\%, \quad (23)$$

$$Error_{Ch1} = \left| \frac{Chl(z) - Chl^{st}(z)}{Chl^{st}(z)} \right| \times 100\%, \quad (24)$$

where,  $\beta_f^{st}$  and  $Chl^{st}$  are the true value of  $\beta_f$  and Chl in the models.

It should be noted that the  $Error_{Chl}$  only considers the errors introduced due to the inaccuracy of  $\beta_f$ , while other errors arising from the inversion model from  $\beta_f$  to Chl are not considered in this calculation.

Based on the aforementioned analysis, the  $Error_\beta$  and  $Error_{Chl}$  for the four different Chl distributions are shown in Fig. 5. As depicted in Fig. 5(a) and Fig. 5(b), when Chl exhibits a monotonic change with depth, whether it increases or decreases, the error increases with depth. However, within a depth of 10 m, both  $Error_\beta$  and  $Error_{Chl}$  remain below 13%. In the other two scenarios, when Chl exhibits a layered distribution with depth, as shown in Fig. 5(c) and Fig. 5(d), even when the Chl concentration range is 0.01 to 10 mg/m<sup>3</sup>, both  $Error_\beta$  and  $Error_{Chl}$  remain below 8%. In conclusion, these results confirm the robustness and reliability of the inversion method.

## 5. Field experiment

### 5.1. Lidar system

As shown in Fig. 6, the single-photon fluorescence lidar system includes four subsystems: a 532 nm pulsed laser, a transceiver, an optical receiver, and a data acquisition system. The system employs a compact fiber-based laser that utilizes a master oscillator power amplifier (MOPA) architecture, incorporating a single-mode pulsed seed laser operating at 1064 nm. The seed laser is amplified through a single-mode ytterbium-doped fiber amplifier (SM-YDFA) and a high-power ytterbium-doped fiber amplifier (HP-YDFA). It then passes through a lithium borate crystal (LBO) for second harmonic generation, achieving an average power output of up to 1.0 W at a wavelength of 532 nm, with a beam divergence of 0.5 mrad. The output pulse width of the laser is 3 ns, and it operates at a repetition frequency of 340 kHz.

To achieve a miniaturized and robust structure, a fiber-connected configuration is specifically designed for the fluorescence lidar system. The backscattered signal from water is coupled into a 105  $\mu$ m multimode fiber (MMF) with a numerical aperture (NA) of 0.22. This coupling is achieved through an achromatic collimator with a 50.8 mm focal length, resulting in a narrow FOV of  $\sim 2.1$  mrad. This narrow FOV not only provides significant suppression of noises but also suppresses multi-scattering components in the backscattered signal. The distance between the transmitted laser and the received collimator is  $\sim 15$  mm.

The backscattered photons are first filtered by a 45° dichroic mirror (DM<sub>2</sub>) to remove the elastic signal at 532 nm and transmit the signal in the 550-750 nm range. The transmitted signals are then separated into the fluorescence channel and the Raman channel using DM<sub>3</sub>. The Raman signal passes through DM<sub>3</sub>, while the fluorescence signal is reflected by DM<sub>3</sub>. The fluorescence backscattered signal is further extracted using a 10 nm bandwidth filter (Filter<sub>1</sub>) centered at 685 nm, while the Raman backscattered signal is extracted using a 6 nm bandwidth filter (Filter<sub>2</sub>) at 650 nm. Finally, the fluorescence channel achieves an isolation degree of 58 dB for the elastic signal, with a transmission of  $\sim 65\%$ . On the other hand, the Raman channel achieves an isolation degree of 55 dB for the elastic signal, with a transmission of  $\sim 60\%$ . Afterward, the fluorescence signal and Raman signal are detected separately using single-photon avalanche diodes (SPADs). Moreover, a self-developed two-channel time-to-digital converter (TDC) with a resolution of 500 ps is employed for the precise acquisition of timing information from the backscattered photons. The electronic module employs a self-constructed function generator (FG) implemented on a field programmable gate array (FPGA) to generate accurate control signals for the laser and TDC. A summary of the system parameters is presented in Table 4.

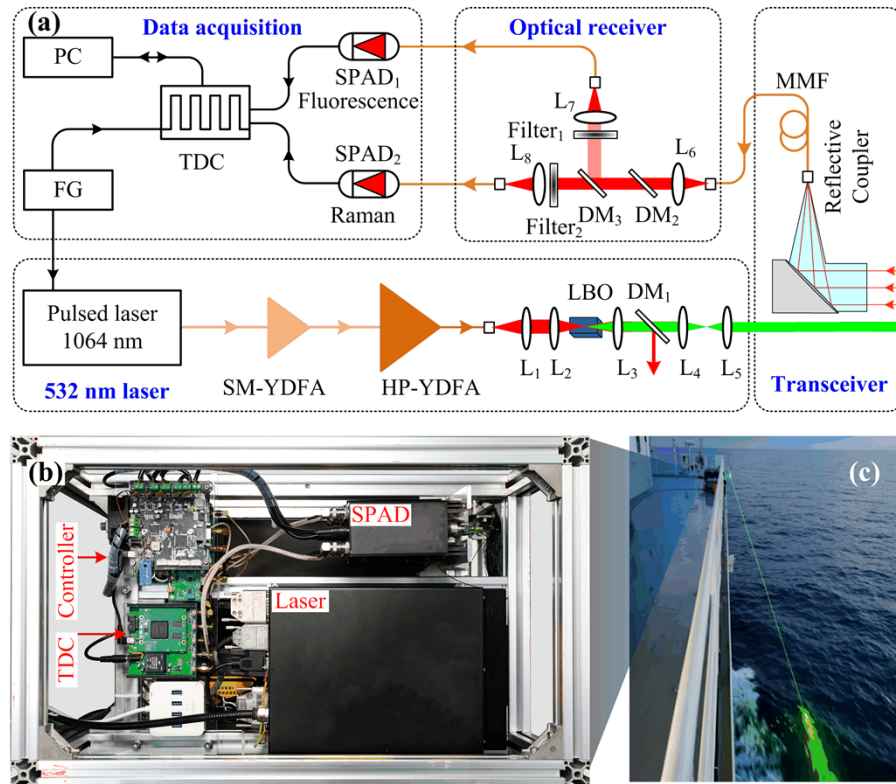


**Fig. 6.** (a) Optical layout of the single-photon fluorescence lidar, (b) interior photo of the lidar system, (c) operational photo of the lidar on the R/V Tan Kah Kee. SM-YDFA: Single-Mode Ytterbium-Doped Fiber Amplifier; HP-YDFA: High-Power Ytterbium-Doped Fiber Amplifier; L: lens; LBO: lithium borate; DM: dichroic mirror; MMF: Multimode fiber; SPAD: single-photon avalanche diode; TDC: time-to-digital converter; FG: function generator; PC: personal computer.

**Table 4. Key parameters of the fluorescence lidar system**

	Parameter	Value
Pulsed laser	Wavelength	532 nm
	Pulse duration	3 ns
	Average power	1 W
	Pulse repetition rate	340 KHz
Collimator	Focal length	50.8 mm
	Mode-field diameter of the MMF	105 $\mu$ m
	Detection efficiency at 650 nm	52%
SAPD	Detection efficiency at 685 nm	48%
	Dark count rate	100 Hz

## 5.2. Field experiment

To verify the stability of the single-photon fluorescence lidar system and the effectiveness of the inversion algorithm, a field experiment was conducted aboard the R/V Tan Kah Kee in the South China Sea from 20:38:04 PM on September 4th to 1:10:54 AM on September 5th, 2022.

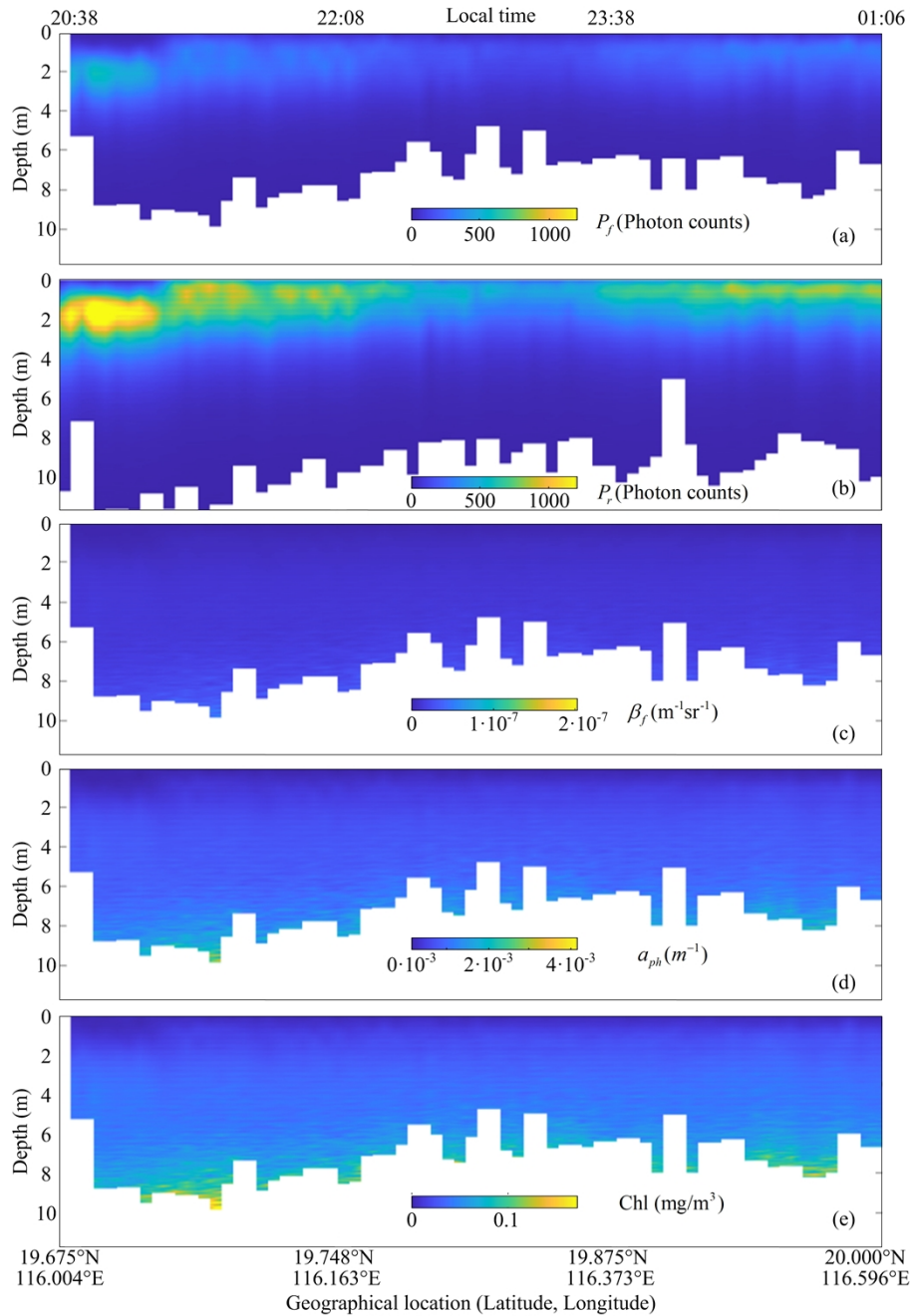


**Fig. 7.** Field experiment results. Raw data  $P_f$  (a),  $P_r$  (b), and inverted results  $\beta_f$  (c),  $a_{ph}$  (d), Chl (e).

The lidar was installed on the deck of the research vessel, positioned  $\sim 15$  m above the water surface, and the laser beam penetrated the water at a near-zenith angle of  $0^\circ$  after being reflected by a mirror located in front of the lidar. The fluorescence lidar collected data with a time resolution of 1 s and a depth resolution of 7.5 cm. To improve the SNR, the time resolution was adjusted to  $\sim 15$  s, and the raw data of  $P_f$  and  $P_r$  are shown in Fig. 7(a) and 7(b) respectively.

From the raw data spanning  $\sim 5$  hours, it can be observed that, by employing of single-photon detection technology, the detection depth of both fluorescence and Raman backscattered signals exceeds 5 m but remains below 10 m. This variation in penetration depth is primarily a result of the laser spot size on the water surface being  $\sim 10$  mm, and the pitching and rolling of the vessel, as well as interference from the air-sea interface, affecting the transmission of the laser through the interface.

Moreover, there are certain fluctuations in the signal intensity of both channels, primarily due to the instability in the output power of the laser. Nevertheless, the fluctuations are practically eliminated when examining the inverted  $\beta_f$  values, as shown in Fig. 7(c). This can be primarily attributed to the normalization of the fluorescence backscattered signal using the Raman backscattered signal, effectively mitigating the influence of laser energy fluctuations. Furthermore, the utilization of a shared transmitter-receiver setup for both channels, combined with the normalization process, eliminates the need for geometric overlap factor correction in the backscattered signal, leading to a significant simplification of the inversion process. This is a crucial advantage of this methodology. During the  $\beta_f$  inversion process,  $\Delta K_{lidar}^{fr0}$  was set to 0.11, and the value of  $B_r/B_f$  was obtained through calibration. The calibration was achieved by attenuating a broadband continuous light source with a known spectral distribution to the single-photon level and coupling it into the optical collimator of the fluorescence lidar system. The ratio of the Raman and fluorescence channel detection signals was then measured to calibrate  $B_r/B_f$ . Furthermore,  $a_{ph}$  and Chl were calculated using the Eq. (13) and Eq. (14) with the values of  $\Phi_c$  of 0.01 [43]. As shown in Fig. 7(d) and Fig. 7(e), the results of  $a_{ph}$  and Chl indicate that in the surveyed ocean during the Tan Kah Kee cruise, the distribution of  $a_{ph}$  and Chl remains relatively stable near the surface. Furthermore, as the depth increases, both  $a_{ph}$  and Chl values show a slight increase, particularly at depths of 8-10 m. From Fig. 7(e), it can be observed that the surface Chl values are  $\sim 0.03$  mg/m<sup>3</sup>, which is consistent with the findings of a previous study in the South China Sea [44].

## 6. Conclusion

In this study, we proposed and demonstrated an algorithm for accurate inversion of the  $\beta_f$  of the fluorescence lidar. Combining empirical models, profiles of  $a_{ph}$  and Chl could be obtained from  $\beta_f$ . To the best of our knowledge, this is the first breakthrough in the retrieval of  $a_{ph}$  and Chl profiles using a fluorescence lidar. This has significant implications for accurately estimating ocean primary productivity, conducting water quality surveys, and studying marine carbon cycles.

In terms of hardware design, by employing a single-photon detector, the detection sensitivity of the fluorescence lidar was improved to the single-photon level. This enabled the detection of fluorescence backscattering profiles of water using a low-pulse-energy laser and a small-aperture telescope system. Additionally, the telescope was designed with a narrow FOV, which reduced the multiple scattering components in the backscattered signal of the lidar.

Regarding the inversion of  $\beta_f$ , it is difficult to simultaneously obtain two parameters, namely  $\beta_f$  and the attenuation coefficient of lidar, from a single lidar measurement. To address this, a water Raman channel was added to the receiving channel. By normalizing the fluorescence backscattering signal with the water Raman backscattering signal, and considering that the 180° backscattering coefficient of water Raman scattering is known, the variation of the difference between the attenuation coefficient of lidar from fluorescence and Raman channels ( $\Delta K_{lidar}^{fr}$ ) and its normalized value with depth was significantly reduced. This allowed for the accurate inversion of  $\beta_f$  based on a perturbation method. Furthermore, normalization also greatly mitigated the influence of laser power fluctuations on the inversion. To determine the range of  $\Delta K_{lidar}^{fr0}$  values and the value to be used in the inversion, a widely used MC method was adopted. Through error analysis, it was found that within a range of 10 m of water depth, even with a variation in Chl from 0.01 to 10 mg/m<sup>3</sup>, the inversion error of  $\beta_f$  was within 13%. Finally, the proposed lidar

system and inversion method were tested in a ~ 5-hour shipborne experiment aboard the R/V Tan Kah Kee, validating the effectiveness of the proposed algorithm and demonstrating the feasibility and efficacy of the fluorescence lidar in practical applications.

In future work, a comparison between the measurements of the fluorescence single-photon lidar and in-situ methods will be conducted to further validate the effectiveness and robustness of the inversion algorithm, which is currently lacking in this study. Additionally, to reduce the influence of chlorophyll fluorescence on the water Raman backscattering signal, the use of shorter wavelength lasers, such as blue lasers, will be considered as the transmitter. Once the influence of chlorophyll fluorescence on the Raman backscattering signal is reduced, the bandwidth of the Raman filters can be further increased to improve the SNR of the Raman backscattering signal. Furthermore, due to the utilization of highly sensitive single-photon detector and a wide bandwidth fluorescence filter, the current single-photon fluorescence lidar is highly susceptible to environmental light. As a result, this lidar system can only operate during nighttime. To enhance the capabilities of the lidar system, the lidar will be upgraded for underwater operation, allowing it to integrate into an autonomous underwater vehicle (AUV) platform. Due to the attenuation of solar radiation in water, the radiation noise reaching the single-photon fluorescence lidar will be significantly reduced. Moreover, by utilizing the AUV platform, the detection of biogeochemical parameters of water bodies from the surface to the deep layers will be accomplished. In conclusion, we believe that this work has significant potential, and the development of this technology will enable scientists to better study marine carbon storage and cycling, facilitating a deeper understanding of the overall role of global carbon cycles and marine ecosystems.

**Funding.** National Key Research and Development Program of China (2022YFB3901704); Joint Funds of the National Natural Science Foundation of China (U2106210); Natural Science Foundation of Fujian Province (No. 2020J01026); MEL-RLAB Joint Fund for Marine Science & Technology Innovation.; Fujian Provincial Central Guided Local Science and Technology Development Special Project (No.2022L3078).

**Acknowledge.** We acknowledge the captain and crew of the R/V Tan Kah Kee for the help during the cruises, particularly Xuewen Wu, Peng Wang, Chengmiao Ye, Jing Dong, and Jiannan Cai.

**Disclosures.** The authors declare no conflicts of interest.

**Data availability.** The data that support the findings of this study are available from the corresponding author upon reasonable request.

## References

1. J. E. O'Reilly, S. Maritorena, B. G. Mitchell, *et al.*, "Ocean color chlorophyll algorithms for SeaWiFS," *J. Geophys. Res.* **103**(C11), 24937–24953 (1998).
2. S. Shang, Z. Lee, G. Lin, *et al.*, "Progressive scheme for blending empirical ocean color retrievals of absorption coefficient and chlorophyll concentration from open oceans to highly turbid waters," *Appl. Opt.* **58**(13), 3359–3369 (2019).
3. A. Bracher, H. A. Bouman, R. J. Brewin, *et al.*, "Obtaining phytoplankton diversity from ocean color: a scientific roadmap for future development," *Front. Mar. Sci.* **4**, 55 (2017).
4. C. Jamet, A. Ibrahim, Z. Ahmad, *et al.*, "Going beyond standard ocean color observations: lidar and polarimetry," *Front. Mar. Sci.* **6**, 251 (2019).
5. J. H. Churnside and J. A. Shaw, "Lidar remote sensing of the aquatic environment," *Appl. Opt.* **59**(10), C92–C99 (2020).
6. L. Sun, Y. Zhang, C. Ouyang, *et al.*, "A portable UAV-based laser-induced fluorescence lidar system for oil pollution and aquatic environment monitoring," *Opt. Commun.* **527**, 128914 (2023).
7. T. Hengstermann and R. Reuter, "Lidar fluorosensing of mineral oil spills on the sea surface," *Appl. Opt.* **29**(22), 3218–3227 (1990).
8. S. R. Rogers, T. Webster, W. Livingstone, *et al.*, "Airborne Laser-Induced Fluorescence (LIF) Light Detection and Ranging (LiDAR) for the quantification of dissolved organic matter concentration in natural waters," *Estuaries Coasts* **35**(4), 959–975 (2012).
9. V. Pelevin, A. Zlinszky, E. Khimchenko, *et al.*, "Ground truth data on chlorophyll-a, chromophoric dissolved organic matter and suspended sediment concentrations in the upper water layer as obtained by LIF lidar at high spatial resolution," *International journal of remote sensing* **38**(7), 1967–1982 (2017).
10. S. C. J. Palmer, V. V. Pelevin, I. Goncharenko, *et al.*, "Ultraviolet Fluorescence LiDAR (UFL) as a Measurement Tool for Water Quality Parameters in Turbid Lake Conditions," *Remote Sens.* **5**(9), 4405–4422 (2013).

11. J. Lu, Y. Yuan, Z. Duan, *et al.*, “Short-range remote sensing of water quality by a handheld fluorosensor system,” *Appl. Opt.* **59**(10), C1–C7 (2020).
12. G. Zhao, M. Ljungholm, E. Malmqvist, *et al.*, “Inelastic hyperspectral lidar for profiling aquatic ecosystems,” *Laser Photonics Rev.* **10**(5), 807–813 (2016).
13. H. H. Kim, “New algae mapping technique by the use of an airborne laser fluorosensor,” *Appl. Opt.* **12**(7), 1454–1459 (1973).
14. Y. Saito, K. Kakuda, M. Yokoyama, *et al.*, “Design and daytime performance of laser-induced fluorescence spectrum lidar for simultaneous detection of multiple components, dissolved organic matter, phycocyanin, and chlorophyll in river water,” *Appl. Opt.* **55**(24), 6727–6734 (2016).
15. M. Shangguan, H. Xia, C. Wang, *et al.*, “Dual-frequency Doppler lidar for wind detection with a superconducting nanowire single-photon detector,” *Opt. Lett.* **42**(18), 3541–3544 (2017).
16. M. Shangguan, H. Xia, C. Wang, *et al.*, “All-fiber upconversion high spectral resolution wind lidar using a Fabry-Perot interferometer,” *Opt. Express* **24**(17), 19322–19336 (2016).
17. C. Yu, M. Shangguan, H. Xia, *et al.*, “Fully integrated free-running InGaAs/InP single-photon detector for accurate lidar applications,” *Opt. Express* **25**(13), 14611–14620 (2017).
18. M. Shangguan, Z. Liao, Y. Guo, *et al.*, “Sensing the profile of particulate beam attenuation coefficient through a single-photon oceanic Raman lidar,” *Opt. Express* **31**(16), 25398–25414 (2023).
19. M. Shangguan, Z. Yang, Z. Lin, *et al.*, “Compact long-range single-photon underwater lidar with high spatial-temporal resolution,” *IEEE Geoscience and Remote Sensing Letters* (2023).
20. M. Shangguan, Z. Yang, M. Shangguan, *et al.*, “Remote sensing oil in water with an all-fiber underwater single-photon Raman lidar,” *Appl. Opt.* **62**(19), 5301–5305 (2023).
21. X. Shen, W. Kong, P. Chen, *et al.*, “A shipborne photon-counting lidar for depth-resolved ocean observation,” *Remote Sens.* **14**(14), 3351 (2022).
22. J. H. Churnside, J. W. Hair, C. A. Hostetler, *et al.*, “Ocean backscatter profiling using high-spectral-resolution lidar and a perturbation retrieval,” *Remote Sens.* **10**(12), 2003 (2018).
23. J. D. Klett, “Stable analytical inversion solution for processing lidar returns,” *Appl. Opt.* **20**(2), 211–220 (1981).
24. F. G. Fernald, “Analysis of atmospheric lidar observations: some comments,” *Appl. Opt.* **23**(5), 652–653 (1984).
25. J. H. Churnside and R. D. Marchbanks, “Inversion of oceanographic profiling lidars by a perturbation to a linear regression,” *Appl. Opt.* **56**(18), 5228–5233 (2017).
26. Y. Zhou, Y. Chen, H. Zhao, *et al.*, “Shipborne oceanic high-spectral-resolution lidar for accurate estimation of seawater depth-resolved optical properties,” *Light: Sci. Appl.* **11**(1), 261 (2022).
27. S. Chen, P. Chen, L. Ding, *et al.*, “A New Semi-Analytical MC Model for Oceanic LIDAR Inelastic Signals,” *Remote Sens.* **15**(3), 684 (2023).
28. J. S. Bartlett, K. J. Voss, S. Sathyendranath, *et al.*, “Raman scattering by pure water and seawater,” *Appl. Opt.* **37**(15), 3324–3332 (1998).
29. L. Zotta, S. Matteoli, M. Diani, *et al.*, “AFRODiTE: A fluorescence LiDAR simulator for underwater object detection applications,” *IEEE Transactions on Geoscience and Remote Sensing* **53**(6), 3022–3041 (2015).
30. C. D. Mobley, *Light and water: radiative transfer in natural waters* (Academic press, 1994).
31. A. Bricaud, M. Babin, A. Morel, *et al.*, “Variability in the chlorophyll-specific absorption coefficients of natural phytoplankton: Analysis and parameterization,” *J. Geophys. Res.* **100**(C7), 13321 (1995).
32. J. Steffens, E. Landulfo, L. C. Courrol, *et al.*, “Application of fluorescence to the study of crude petroleum,” *J. Fluoresc.* **21**(3), 859–864 (2011).
33. D. J. Spence, B. R. Neimann, and H. M. Pask, “Monte Carlo modelling for elastic and Raman signals in oceanic LiDAR,” *Opt. Express* **31**(8), 12339–12348 (2023).
34. T. J. Petzold, “Volume scattering functions for selected ocean waters,” (Scripps Institution of Oceanography La Jolla Ca Visibility Lab, 1972).
35. Z. Lee and J. Tang, “The two faces of “Case-1” water,” *Journal of Remote Sensing* (2022).
36. A. Morel, “Optical properties of pure water and pure seawater,” *Optical aspects of oceanography* (1974).
37. A. Morel, “Optical modeling of the upper ocean in relation to its biogenous matter content (case I waters),” *J. Geophys. Res.: Oceans* **93**(C9), 10749–10768 (1988).
38. L. Prieur and S. Sathyendranath, “An optical classification of coastal and oceanic waters based on the specific spectral absorption curves of phytoplankton pigments, dissolved organic matter, and other particulate materials 1,” *Limnol. Oceanogr.* **26**(4), 671–689 (1981).
39. R. P. Souto, P. L. Silva Dias, H. F. Campos Velho, *et al.*, “New developments on reconstruction of high resolution chlorophyll-a vertical profiles,” *Comp. Appl. Math.* **36**(3), 1195–1204 (2017).
40. C. D. Mobley and S. S. I. B. Wa, “Ecosystem Predictions with Approximate vs. Exact Light Fields,” (2009).
41. H. Loisel, D. Stramski, B. G. Mitchell, *et al.*, “Comparison of the ocean inherent optical properties obtained from measurements and inverse modeling,” *Appl. Opt.* **40**(15), 2384–2397 (2001).
42. J. Sánchez-España, C. Falagán, D. Ayala, *et al.*, “Adaptation of *Coccomyxa* sp. to extremely low light conditions causes deep chlorophyll and oxygen maxima in acidic pit lakes,” *Microorganisms* **8**(8), 1218 (2020).
43. S. Maritorena, A. Morel, and B. Gentili, “Determination of the fluorescence quantum yield by oceanic phytoplankton in their natural habitat,” *Appl. Opt.* **39**(36), 6725–6737 (2000).

44. S. Shen, G. G. Leptoukh, J. G. Acker, *et al.*, "Seasonal variations of Chlorophyll a concentration in the Northern South China Sea," *IEEE Geosci. Remote Sensing Lett.* **5**, 315–319 (2008).